Nanoscale determination of interatomic distance by ptychography-EXAFS method using advanced Kirkpatrick-Baez mirror focusing optics

doi: 10.1107/S1600577519017004

research paper

JOURNAL OF SYNCHROTRON RADIATION

ISSN 1600-5775

Nanoscale determination of interatomic distance by ptychography-EXAFS method using advanced Kirkpatrick–Baez mirror focusing optics

Makoto Hirose,[a,b]* Kei Shimomura,[a,b] Takaya Higashino,[a,b] Nozomu Ishiguro[b,c] and Yukio Takahashi[a,b,c]*

[a]Graduate School of Engineering, Osaka University, 2-1 Yamada-oka, Suita, Osaka 565-0855, Japan, [b]RIKEN SPring-8 Center, 1-1-1 Kouto, Sayo-cho, Sayo, Hyogo 679-5148, Japan, and [c]Institute of Multidisciplinary Research for Advanced Materials (IMRAM), Tohoku University, Sendai, Miyagi 980-8577, Japan. *Correspondence e-mail: hirose@up.prec.eng.osaka-u.ac.jp, ytakahashi@tohoku.ac.jp

Received 10 April 2019
Accepted 19 December 2019

Edited by V. Favre-Nicolin, CEA and Université Joseph Fourier, France

Keywords: X-ray ptychography; X-ray absorption fine structure; Kirkpatrick–Baez; advanced Kirkpatrick–Baez mirrors.

This work demonstrates a combination technique of X-ray ptychography and the extended X-ray absorption fine structure (ptychography-EXAFS) method, which can determine the interatomic distances of bulk materials at the nanoscale. In the high-resolution ptychography-EXAFS method, it is necessary to use high-intense coherent X-rays with a uniform wavefront in a wide energy range, hence a ptychographic measurement system installed with advanced Kirkpatrick–Baez mirror focusing optics is developed and its performance is evaluated. Ptychographic diffraction patterns of micrometre-size MnO particles are collected by using this system at 139 energies between 6.504 keV and 7.114 keV including the Mn *K* absorption edge, and then the EXAFS of MnO is derived from the reconstructed images. By analyzing the EXAFS spectra obtained from a 48 nm × 48 nm region, the nanoscale bond lengths of the first and second coordination shells of MnO are determined. The present approach has great potential to elucidate the unclarified relationship among the morphology, electronic state and atomic arrangement of inhomogeneous bulk materials with high spatial resolution.

1. Introduction

The extended X-ray absorption fine structure (EXAFS), *i.e.* the oscillatory modulation of the absorption coefficient on the high-energy side of an X-ray absorption edge, is used for probing the interatomic distance and coordination number of X-ray absorbing atoms in materials without long-range order. In particular, owing to the availability of highly brilliant synchrotron X-rays, the technique has been successfully applied to various forms of matter: gases, liquids, solutions, nanoparticles, polycrystalline and amorphous materials, contributing to great progress in chemistry and materials science (Teo, 1986; Eisenberger & Kincaid, 1978). One of the most important targets of EXAFS spectroscopy are heterogeneous functional materials whose local structures are not uniform at the nanoscale. Most EXAFS data, however, are taken as a macroscopic average over the entire illumination field, which is typically of the order of millimetres. The nanoscale structural inhomogeneity is averaged in the conventional approaches, though knowledge of the spatial distribution of structural differences at the nanoscale is of considerable importance for designing better functional materials.

The combination of EXAFS spectroscopy and X-ray microscopy is expected to facilitate the study of structural

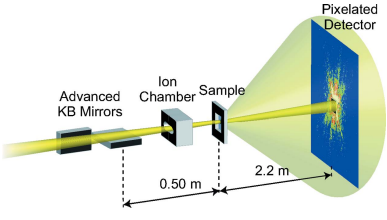

variation inside bulk matter with nanoscale spatial resolution. Thus far, scanning transmission X-ray microscopy (STXM) has been used for EXAFS analysis (Takao *et al.*, 2014, 2015, 2018; Segura-Ruiz *et al.*, 2011; Martínez-Criado *et al.*, 2014*a*,*b*). Here the spatial resolution is, in principle, restricted by the focal spot size, namely the fabrication quality of the X-ray lens, which is approaching its technical limitation. An alternative method of determining the atomic arrangement with a much higher spatial resolution is electron energy-loss spectroscopy (EELS) performed in an aberration-corrected transmission electron microscopy (TEM) system (Egerton, 2009). In TEM-EELS, an extended energy-loss fine structure (EXELFS) likewise offers structural information based on an analogous theory to EXAFS. However, the sample must be thinned to 10 nm due to the small penetration depth of electrons.

X-ray ptychography, which is a scanning type of lensless imaging using coherent X-rays, is a promising approach to achieving high spatial resolution beyond the limitation imposed by the X-ray optics since the resolution is determined by the maximum angular extent of the scattered photons (Rodenburg *et al.*, 2007; Thibault *et al.*, 2008). A ptychographic dataset, comprising multiple coherent X-ray diffraction patterns recorded with a step width smaller than the illumination size, produces sufficient redundancy for iteratively solving the inversion problem to recover a complex transmission function of a specimen. Furthermore, a complex-valued illumination field of incident X-rays can also be determined owing to the development of the phase retrieval algorithm (Maiden & Rodenburg, 2009; Thibault *et al.*, 2009). Recently, the X-ray absorption fine structure (XAFS) has been derived from the reconstructed complex transmission functions in both soft and hard X-ray regimes (Beckers *et al.*, 2011; Shapiro *et al.*, 2014; Yu *et al.*, 2015, 2018; Wise *et al.*, 2016; Farmand *et al.*, 2017; Hirose *et al.*, 2017, 2018, 2019), *i.e.* ptychography-XAFS, which provides chemical and magnetic information at the nanoscale. However, ptychography-XAFS experiments have been limited to the X-ray absorption near-edge structure (XANES) region owing to experimental difficulties.

Kirkpatrick–Baez (KB) mirrors, *i.e.* a pair of one-dimensional focusing mirrors with an elliptic surface, are suitable focusing optics for spectromicroscopy experiments because of their achromatic property and high reflectivity. However, both the wavefront and focal position are sensitive to variations of the incidence angle owing to the comatic aberration (Matsuyama *et al.*, 2006), which would be a crucial problem in the ptychography-EXAFS method since it requires long measurement times. To suppress the positional drift of the focused beam, a nanopositioning system installed with KB mirrors with a short working distance has been developed at the European Synchrotron Radiation Facility (Villar *et al.*, 2018). However, the setup often limits the application, requiring a large space for the sample in cases such as *in situ* measurements. To provide focused coherent X-rays with a uniform wavefront in a wide energy range, advanced KB (AKB) mirror focusing optics with a long working distance are promising as illumination optics. AKB mirrors consist of a pair of one-dimensional focusing mirrors with elliptic and hyperbolic surfaces, *i.e.* one-dimensional Wolter mirrors, which can greatly suppress the comatic aberration (Kodama *et al.*, 1996). Recently, high-resolution full-field imaging in the hard X-ray region with long-term stability was reported (Matsuyama *et al.*, 2017). Use of AKB mirrors as the focusing optics is expected to provide long-term stability also in scanning microscopy. This is important in time-consuming measurements such as the ptychography-EXAFS method.

In this study, we developed a ptychographic measurement system with AKB mirrors installed as illumination optics and evaluated its performance. Then, we performed ptychography-EXAFS measurements on micrometre-size MnO particles using this system. In this article, we determine the interatomic distances of the first and second coordination shells with sub-50 nm spatial resolution, and then quantitatively evaluate the noise level of ptychography-EXAFS and, finally, we compare this technique with other X-ray micro/nanospectroscopy techniques.

Table 1
Parameters of the designed AKB mirrors.

Coefficients a and b are from the equations of an ellipse $x^2/a^2 + y^2/b^2 = 1$ or hyperbola $x^2/a^2 - y^2/b^2 = 1$. The incident glancing angle and the distance from the focus are measured at the center of the mirrors. The mirror area length denotes the distance along the X-ray axis.

	Ellipse (H)	Hyperbola (H)	Ellipse (V)	Hyperbola (V)
a (m)	24.7	0.367	24.6	0.251
b (m)	2.61×10^{-2}	3.10×10^{-3}	2.25×10^{-2}	2.16×10^{-3}
Incident glancing angle (mrad)	3.04	3.08	3.09	3.06
Distance from focus (mm)	811	706	602	500
Mirror area length (mm)	99.0	93.7	97.5	90.2

2. Performance test of AKB mirror optics for X-ray ptychography

The design parameters of the AKB mirrors (JTEC Corporation) are summarized in Table 1. The working distance is 0.45 m. The mirror figures were fabricated on Si substrates by computer-controlled elastic emission machining (Yamauchi *et al.*, 2002). The figure error is less than 2 nm peak-to-valley, and the surface roughness is less than 0.3 nm root mean square. No surface coating is performed on these mirrors. X-ray energies of up to 10 keV can be utilized with 90% reflectivity for a single reflection of the Si surface. The reflectivity of the AKB mirrors drops to 66% at 10 keV since the mirrors involve four reflections.

The performance test of the AKB mirror optics was carried out at the SPring-8 BL29XUL beamline (Tamasaku *et al.*, 2001). A schematic of the experimental setup is given in Fig. 1. The distance between the light source and the Si (111) double-crystal monochromator is 43 m. The distance between the

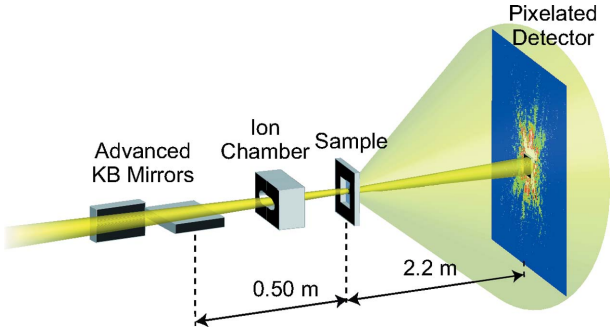

Figure 1
Schematic of the ptychographic measurement system installed with AKB mirrors as a focusing device at the SPring-8 BL29XUL beamline. The experimental hutch has a temperature feedback system to suppress the temperature drift to less than 0.05 K. The distance between the center of the downstream hyperbolic mirror and the focal point is 0.50 m. The working distance is 0.45 m. The AKB mirror unit is purged with He gas. To monitor the intensity of the incident X-rays, an ion chamber is placed between the mirror and the sample. Diffraction intensities are normalized by the incident flux at each scan position. The sample is mounted on nanopositioning piezoelectric stages in a vacuum chamber with less than 0.1 Pa pressure. A semitransparent Si beamstop is placed in front of the detector. The diffraction patterns are measured by a pixelated detector (EIGER 1M) placed 2.2 m downstream of the sample plane.

monochromator and the sample is 55 m. A slit with a 10 μm × 30 μm aperture was installed 50 m upstream of the sample plane to offer fully coherent X-rays. Incident X-rays were monochromated to 6.5 keV, and then two-dimensionally focused onto a sample placed at the focal plane. In this setup, the incident flux at the sample plane was approximately 2×10^8 photons s^{-1}. A 200 nm-thick Ta Siemens star pattern was raster-scanned in 15 × 15 points with a 200 nm step size. Far-field coherent X-ray diffraction patterns were captured by an in-vacuum hybrid pixelated detector EIGER 1M (Dectris) with a 75 μm × 75 μm pixel size (Johnson *et al.*, 2014). An 88 μm-thick semitransparent Si beamstop with an intensity transmittance of 0.1 for 6.5 keV X-rays was installed in front of the detector to attenuate the transmitted direct beam and effectively increase the dynamic range of diffraction intensity. In this experimental setup, the pixel size of the reconstructed image was 7.6 nm.

To evaluate the positional stability of the X-ray beam spot focused by the AKB mirrors, the positional correction method was performed in the ptychography measurement (Takahashi *et al.*, 2011). Fig. 2(*a*) shows the time dependence of the focal position along the horizontal and vertical directions. The peak-to-peak position was 43.3 nm in the horizontal direction and 65.1 nm in the vertical direction over 7 h. The average amounts of drift at each scan were 1.9 nm in the horizontal direction and 5.0 nm in the vertical direction. Figs. 2(*b*) and 2(*c*) show the sample and probe images, respectively, reconstructed by the ePIE algorithm (Maiden & Rodenburg, 2009). The smallest 50 nm structure in the test sample was sharply resolved. The results show that the present measurement system has sufficient stability for high-resolution X-ray ptychography even with the long-working-distance mirror optics.

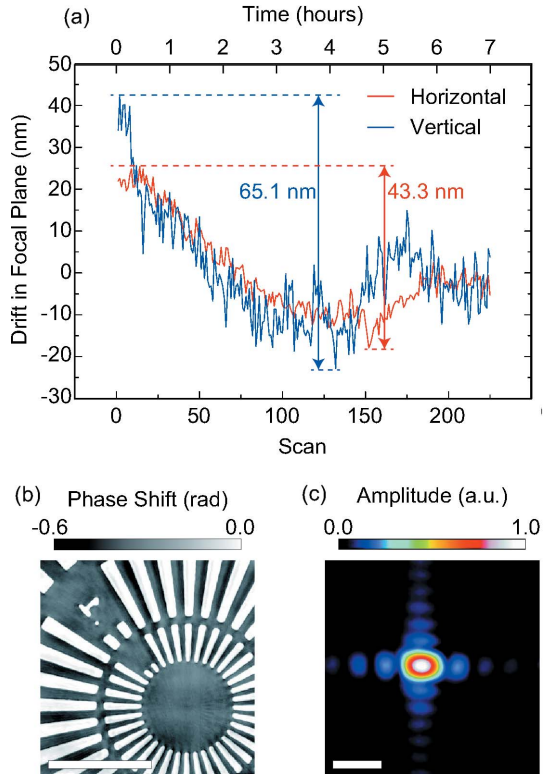

Figure 2
(*a*) Amount of drift of the focal position during the ptychography measurement in the horizontal and vertical directions. (*b*) Phase image of the test sample (scale bar represents 1 μm). (*c*) Amplitude image of the focused illumination field produced by the AKB mirrors (scale bar represents 1 μm).

3. Ptychography-EXAFS measurement of MnO particles

3.1. Experiment and reconstruction

A ptychography-EXAFS experiment was performed to determine the bond lengths of MnO particles. The geometrical parameters of the beamline including the AKB mirror focusing system were the same as those in the performance test. The MnO particles were dispersed in ethanol solution, then the suspension was dropped on a 500 nm-thick Si_3N_4 membrane chip (Norcada) and dried in air. An FE-SEM (HITACHI, S-4800) image of the prepared sample is shown in Fig. 3(*a*). Coherent X-rays were tuned to 139 energies between 6.504 keV and 7.114 keV including the Mn *K* absorption edge (6.539 keV), and the smallest energy gap was 1 eV in the vicinity of the absorption edge. The particles were scanned over 14 × 14 points with 250 nm separation and 4.0 s exposure. Under these experimental conditions, the total number of measured diffraction patterns was 27 224. The total acquisition time was almost 3 days, including the determination of the scan area at each X-ray energy, the energy scan and experimental interruptions. Note that the AKB mirrors were not realigned during the measurement.

To reconstruct weak XAFS signals in the hard X-ray region, the ePIE algorithm with the dispersion relation as an additional pixelwise constraint is effective for the quantitative

reconstruction (Hirose *et al.*, 2017). Fig. 3(*b*) shows one of the ptychographic diffraction patterns at 6.504 keV. The region of interest of the diffraction patterns was adjusted to uniformly set the pixel size in real space to 12 nm at all X-ray energies. In the image reconstruction, the initial object functions were unity at all X-ray energies, and the initial probe functions were the ideal wavefield calculated using the parameters of the AKB mirrors. The dispersion relation involves an integral with an infinite interval. To suppress the calculation error by the finite interval integral of the experimentally obtainable EXAFS spectra, the dispersion constraint was applied every 100 iterations. In the constraint, spline interpolation was applied when converting the spectra. This procedure was repeated until the sample and probe functions were reconstructed with good convergence at all X-ray energies. The absorption image $\mu t(\mathbf{r}, E)$, *i.e.* the two-dimensional distribution of optical density, is defined as

$$\mu t(\mathbf{r}, E) = -2 \log | T(\mathbf{r}, E) | , \quad (1)$$

where $T(\mathbf{r}, E)$ is the complex transmission function of the sample, $\mathbf{r}$ is the real-space coordinate and E is the X-ray energy.

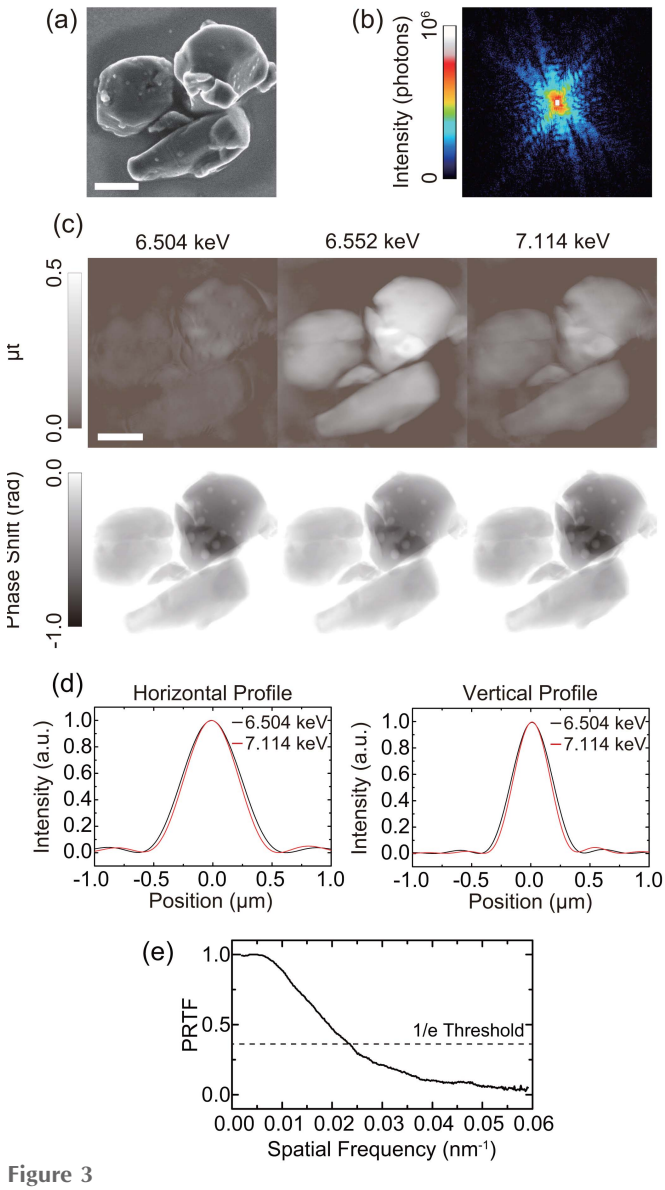

Figure 3
(*a*) FE-SEM image of MnO particles (scale bar represents 1 μm). (*b*) Diffraction pattern at 6.504 keV. The central area including the bright field is attenuated by a factor of 0.1. (*c*) Absorption (upper) and phase (lower) images at 6.504 keV, 6.552 keV and 7.114 keV (scale bar represents 1 μm). (*d*) Horizontal (H) and vertical (V) focal intensity profiles at 6.504 keV and 7.114 keV. Gaussian fitting analysis shows that the full width at half-maximum beam sizes are 444 nm (H) by 311 nm (V) at 6.504 keV and 408 nm (H) by 280 nm (V) at 7.114 keV. (*e*) PRTF analysis of the reconstructed MnO particles at 6.552 keV. The full-period spatial resolution is determined to be 43.6 nm from the intersection of the 1/e threshold.

3.2. Results

Fig. 3(*c*) shows the reconstructed μt and phase images of the sample at 6.504 keV, 6.552 keV and 7.114 keV, which show good morphological agreement with the FE-SEM image in Fig. 3(*a*). The intensity profiles of the probe functions are also presented in Fig. 3(*d*). The presence of the absorption peak of MnO was clearly confirmed at 6.552 keV, whereas clear contrast is not observed in the phase images since the phase spectrum does not show a peak at the three energies. The full-period spatial resolution was estimated to be 43.6 nm by phase retrieval transfer function (PRTF) analysis (Chapman *et al.*, 2006) at 6.552 keV as shown in Fig. 3(*e*).

Fig. 4(*a*) shows an enlarged μt map of the thickest MnO particle (the upper-right particle in the FE-SEM image) at 6.552 keV. Figs. 4(*b*) and 4(*c*) show spatially resolved EXAFS and phase spectra, respectively, which were extracted from a 720 nm × 720 nm or 48 nm × 48 nm region. Clear energy dispersion is observed in not only the absorption spectra but also the phase spectra. EXAFS analysis was performed using the *Ifeffit* program (*Athena* and *Artemis*) (version 0.9.25; Ravel & Newville, 2005). First, the background subtraction and normalization of the raw spectra were performed using the *Athena* program, then the k^3-weighted EXAFS functions were calculated as presented in Fig. 4(*d*). The EXAFS functions between 3.0 Å^{-1} and 10.0 Å^{-1} in k-space were converted to radial distribution functions (RDFs) in R-space as shown in Fig. 4(*e*). Two peaks representing the first Mn—O coordination shell and the second Mn—Mn coordination shell are recognized. At first, curve-fitting analysis of the EXAFS function at position (i) for the reference data was carried out in the range 1.1–3.3 Å in R-space in consideration of the single scattering of the first and second shells. In this fitting analysis, the coordination numbers were set to 6 and 12, respectively, on the basis of the space group $Fm\bar{3}m$ of the MnO particles. The experimental curves showed good agreement with the fitted curves in both k-space and R-space. The results of the EXAFS analysis at position (i) are given in Table 2. Here, the reference interatomic distances determined by X-ray diffraction are 2.22 Å for the first-neighbor Mn—O bond and 3.14 Å for the second-neighbor Mn—Mn bond (Sasaki *et al.*, 1980). Next, the interatomic distances of nanoscale EXAFS at positions (ii)–(iv) were analyzed in the same k and R regions

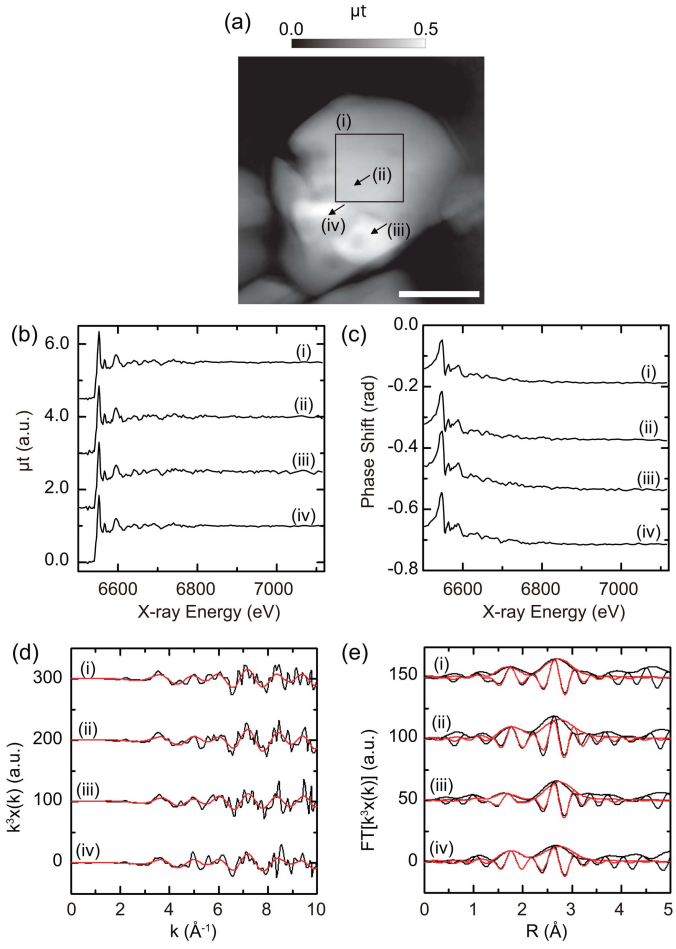

Figure 4
(*a*) Enlarged absorption image at 6.552 keV (scale bar represents 1 μm). (*b*) EXAFS spectra after background subtraction and normalization. The EXAFS spectrum at position (i) is obtained from a 720 nm × 720 nm area, and the other spectra are obtained from 48 nm × 48 nm areas. (*c*) Phase spectra at the same positions as in (*b*). For clarity, phase spectra (ii), (iii) and (iv) are shifted by −0.15 rad, −0.30 rad and −0.45 rad, respectively. (*d*) k^3-Weighted EXAFS functions. (*e*) Magnitude and real part of RDF. Black curves denote the experimental data and red curves denote the fitted curves.

using the predetermined S_0^2 and ΔE as shown in Table 3. All the estimated interatomic distances are similar to the reference values. For simultaneous determination of the coordination number and Debye–Waller factor, further improvement of the signal-to-noise ratio with a higher-energy range is necessary.

3.3. Discussion

It was reported by Belli *et al.* (1980) that a pre-edge structure appeared in the MnO XANES spectrum. The intensity of the pre-edge peak, which is sensitive to the structural symmetry, is less than 10% of that of the white line. Fig. 5(*a*) shows an enlarged view of the XANES spectra reconstructed by the ptychography-EXAFS method. It is difficult to completely distinguish the pre-edge structures from the noise level. The dominant noise source in the ptychography-EXAFS method is photon shot noise. The noise level in the absorption

Table 2
Fitting results of the standard EXAFS.

Coordination number is set to 6 for Mn—O bonds and 12 for Mn—Mn bonds. R_f is the *R*-factor. $S_0^2 = 0.791 \pm 0.261$, $\Delta E = -2.36 \pm 2.80$ (eV).

Shell	*R* (Å)	$\sigma^2 \times 10^{-3}$ (Å^2)
Position (i), $R_f = 0.0405$		
Mn—O	2.24 ± 0.023	1.80 ± 3.76
Mn—Mn	3.15 ± 0.021	6.01 ± 2.92

Table 3
Fitting results of the nanoscale EXAFS.

S_0^2 and ΔE are given in Table 2.

Shell	Coordination No.	*R* (Å)	$\sigma^2 \times 10^{-3}$ (Å^2)
Position (ii), $R_f = 0.115$			
Mn—O	4.20 ± 3.95	2.26 ± 0.024	−3.69 ± 7.75
Mn—Mn	7.30 ± 5.76	3.15 ± 0.014	1.04 ± 6.20
Position (iii), $R_f = 0.0673$			
Mn—O	6.10 ± 5.45	2.22 ± 0.036	8.19 ± 11.2
Mn—Mn	10.2 ± 4.80	3.15 ± 0.010	5.13 ± 3.90
Position (iv), $R_f = 0.0537$			
Mn—O	3.58 ± 2.06	2.25 ± 0.015	−3.34 ± 4.69
Mn—Mn	10.7 ± 5.00	3.16 ± 0.010	6.45 ± 4.10

image is determined by the root mean square error outside the sample area where μt is zero independent of the X-ray energy as follows,

$$\mu t_{\rm noise} = \frac{1}{N}\sum_{j=1}^{N}\left[\frac{1}{M}\sum_{\mathbf{r}\notin S}|\mu t(\mathbf{r}, E_j)|^2\right]^{1/2}, \qquad (2)$$

where S represents the sample area (*i.e.* the support), M represents the number of pixels outside the support area and N represents the number of the X-ray energy. The support area was determined by the 0 rad threshold of the 5-pixel blurred phase image at 6.504 keV as shown in Fig. 5(*b*). The noise level was determined to be 0.013, which is equivalent to the signal level of the pre-edge peak of MnO.

To accurately reconstruct the weak XAFS signals such as the pre-edge structure and/or EXAFS at a higher energy, further improvement of the signal-to-noise ratio of the nanoscale XAFS spectrum is required. Fluorescence detection is frequently used to obtain the weak XAFS signals with high sensitivity from dilute and thin samples. In an STXM system using a micrometre-sized beam focused by KB mirrors, the EXAFS analysis of a micrometre-sized single catalyst particle was performed (Tada *et al.*, 2011). Furthermore, the structure of a single nanowire was also determined with 100 nm spatial resolution (Segura-Ruiz *et al.*, 2011). This approach can be applied to the ptychography-EXAFS method by introducing a fluorescence X-ray detector, in which the spatial resolution of a fluorescence image can be improved by deconvoluting the reconstructed probe intensity (Vine *et al.*, 2012; Deng *et al.*, 2017), then high-resolution fluorescence EXAFS spectra are in principle obtained. Such nanoscale fluorescence EXAFS spectra would be helpful information to improve the signal-to-noise ratio of ptychography-EXAFS data by using the spectra

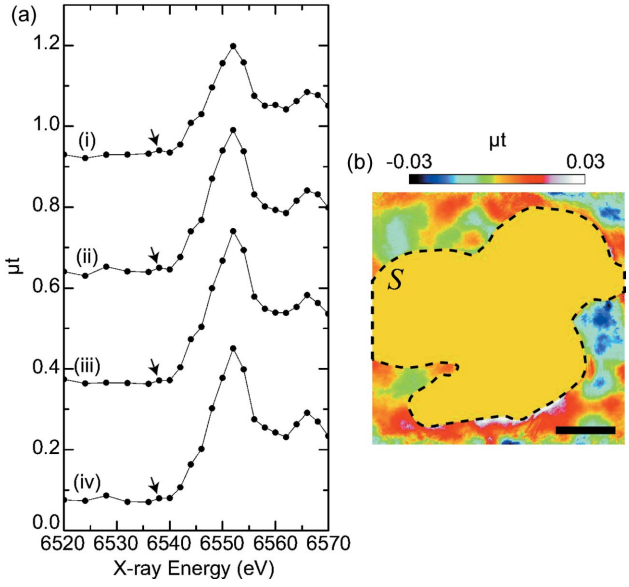

Figure 5
(*a*) Enlarged views of the XANES region in the EXAFS spectra before normalization and background subtraction. The XANES spectra are obtained from the same positions as in Fig. 4. For clarity, raw XANES spectra (i), (ii) and (iii) are shifted by 0.90, 0.60 and 0.30, respectively. The pre-edge structure of the MnO XANES is indicated by the arrows. (*b*) Absorption image at 6.540 keV and the support area. The dashed line is the boundary of the support area; the absorption inside the support area is set to 0 to highlight the noise level outside the support area (scale bar represents 1 μm).

as a spectral constraint, even though the spatial resolution of the ptychograhy is finer than that of the deconvoluted fluorescence map.

Currently, the available flux of incident X-rays for the ptychography-XAFS method is limited for the present synchrotron light source since X-ray ptychography experiments require highly coherent X-rays. In near-future synchrotron facilities, the coherent X-ray flux will be increased by a few orders of magnitude, which will open up the possibility of visualization of spatiotemporal chemical reactions and structural heterogeneities at an unprecedented high spatial resolution.

4. Conclusions

In this study, we expanded the X-ray energy range used for the ptychography-XAFS method to the EXAFS region to determine interatomic distances at the nanoscale. To provide stable X-ray illumination in the time-consuming ptychography-EXAFS method, a ptychographic measurement system equipped with AKB mirrors as focusing optics was developed. In the present setup, the accumulated drift was suppressed to 43.3 nm in the horizontal direction and 65.1 nm in the vertical direction for 7 h. To further improve the positional stability within the setup, the temperature in our apparatus must be controlled with a higher precision.

The ptychography-EXAFS measurement of MnO particles was carried out using the Mn *K*-absorption edge. Image recovery was successfully demonstrated with sub-50 nm spatial resolution without mirror realignment over 3 days, and then the nanoscale EXAFS spectra were obtained. The bond lengths of the first Mn—O coordination shell and the second Mn—Mn coordination shell showed good agreement with the reference bond lengths. The noise level of the presented ptychography-EXAFS method was equivalent to the signal level of the pre-edge peak of MnO. Probe deconvolution of the fluorescence map was proposed as a method for improving the signal-to-noise ratio of ptychography-EXAFS.

The ptychography-EXAFS method has great potential to correlate the interatomic distance, coordination number, chemical state, symmetry and surface morphology in real space with high spatial resolution. We believe that the present approach provides a novel opportunity to investigate complex systems such as catalysts, batteries, rubber, magnetic materials and nanoparticles in biological specimens.

Acknowledgements

We thank T. Ishikawa and K. Endo for many stimulating discussions, as well as Y. Kohmura for his help in the synchrotron experiment.

Funding information

This work was supported by the Japan Society for the Promotion of Science (JSPS) KAKENHI (Grant Nos. JP16J00329, JP17J01673, JP18H05253 and JP19H05814). This work was also supported in part by "Dynamic Alliance for Open Innovation Bridging Human, Environment and Materials" from the Ministry of Education, Culture, Sports, Science and Technology of Japan (MEXT).

References

Beckers, M., Senkbeil, T., Gorniak, T., Reese, M., Giewekemeyer, K., Gleber, S.-C., Salditt, T. & Rosenhahn, A. (2011). *Phys. Rev. Lett.* **107**, 208101.
Belli, M., Scafati, A., Bianconi, A., Mobilio, S., Palladino, L., Reale, A. & Burattini, E. (1980). *Solid State Commun.* **35**, 355–361.
Chapman, H. N., Barty, A., Marchesini, S., Noy, A., Hau-Riege, S. P., Cui, C., Howells, M. R., Rosen, R., He, H., Spence, J. C. H., Weierstall, U., Beetz, T., Jacobsen, C. & Shapiro, D. A. (2006). *J. Opt. Soc. Am. A*, **23**, 1179–1200.
Deng, J., Vine, D. J., Chen, S., Jin, Q., Nashed, Y. S. G., Peterka, T., Vogt, S. & Jacobsen, C. (2017). *Sci. Rep.* **7**, 445.
Egerton, R. F. (2009). *Rep. Prog. Phys.* **72**, 016502.
Eisenberger, P. & Kincaid, B. M. (1978). *Science*, **200**, 1441–1447.
Farmand, M., Celestre, R., Denes, P., Kilcoyne, A. L. D., Marchesini, S., Padmore, H., Tyliszczak, T., Warwick, T., Shi, X., Lee, J., Yu, Y.-S., Cabana, J., Joseph, J., Krishnan, H., Perciano, T., Maia, F. R. N. C. & Shapiro, D. A. (2017). *Appl. Phys. Lett.* **110**, 063101.
Hirose, M., Ishiguro, N., Shimomura, K., Burdet, N., Matsui, H., Tada, M. & Takahashi, Y. (2018). *Angew. Chem.* **130**, 1490–1495.
Hirose, M., Ishiguro, N., Shimomura, K., Nguyen, D.-N., Matsui, H., Dam, H. C., Tada, M. & Takahashi, Y. (2019). *Commun. Chem.* **2**, 50.
Hirose, M., Shimomura, K., Burdet, N. & Takahashi, Y. (2017). *Opt. Express*, **25**, 8593–8603.
Johnson, I., Bergamaschi, A., Billich, H., Cartier, S., Dinapoli, R., Greiffenberg, D., Guizar-Sicairos, M., Henrich, B., Jungmann, J., Mezza, D., Mozzanica, A., Schmitt, B., Shi, X. & Tinti, G. (2014). *J. Instrum.* **9**, C05032.

Kodama, R., Ikeda, N., Kato, Y., Katori, Y., Iwai, T. & Takeshi, K. (1996). *Opt. Lett.* **21**, 1321–1323.
Maiden, A. M. & Rodenburg, J. M. (2009). *Ultramicroscopy*, **109**, 1256–1262.
Martínez-Criado, G., Segura-Ruiz, J., Alén, B., Eymery, J., Rogalev, A., Tucoulou, R. & Homs, A. (2014*a*). *Adv. Mater.* **26**, 7873–7879.
Martínez-Criado, G., Segura-Ruiz, J., Chu, M.-H., Tucoulou, R., López, I., Nogales, E., Mendez, B. & Piqueras, J. (2014*b*). *Nano Lett.* **14**, 5479–5487.
Matsuyama, S., Mimura, H., Yumoto, H., Sano, Y., Yamamura, K., Yabashi, M., Nishino, Y., Tamasaku, K., Ishikawa, T. & Yamauchi, K. (2006). *Rev. Sci. Instrum.* **77**, 103102.
Matsuyama, S., Yasuda, S., Yamada, J., Okada, H., Kohmura, Y., Yabashi, M., Ishikawa, T. & Yamauchi, K. (2017). *Sci. Rep.* **7**, 46358.
Ravel, B. & Newville, M. (2005). *J. Synchrotron Rad.* **12**, 537–541.
Rodenburg, J. M., Hurst, A. C., Cullis, A. G., Dobson, B. R., Pfeiffer, F., Bunk, O., David, C., Jefimovs, K. & Johnson, I. (2007). *Phys. Rev. Lett.* **98**, 034801.
Sasaki, S., Fujino, K., Takéuchi, Y. & Sadanaga, R. (1980). *Acta Cryst.* A**36**, 904–915.
Segura-Ruiz, J., Martínez-Criado, G., Chu, M. H., Geburt, S. & Ronning, C. (2011). *Nano Lett.* **11**, 5322–5326.
Shapiro, D. A., Yu, Y.-S., Tyliszczak, T., Cabana, J., Celestre, R., Chao, W., Kaznatcheev, K., Kilcoyne, A. L. D., Maia, F., Marchesini, S., Meng, Y. S., Warwick, T., Yang, L. L. & Padmore, H. A. (2014). *Nat. Photon.* **8**, 765–769.
Tada, M., Ishiguro, N., Uruga, T., Tanida, H., Terada, Y., Nagamatsu, S., Iwasawa, Y. & Ohkoshi, S. (2011). *Phys. Chem. Chem. Phys.* **13**, 14910–14913.
Takahashi, Y., Suzuki, A., Zettsu, N., Kohmura, Y., Senba, Y., Ohashi, H., Yamauchi, K. & Ishikawa, T. (2011). *Phys. Rev. B*, **83**, 214109.
Takao, S., Sekizawa, O., Nagamatsu, S., Kaneko, T., Yamamoto, T., Samjeské, G., Higashi, K., Nagasawa, K., Tsuji, T., Suzuki, M., Kawamura, N., Mizumaki, M., Uruga, T. & Iwasawa, Y. (2014). *Angew. Chem. Int. Ed.* **53**, 14110–14114.
Takao, S., Sekizawa, O., Samjeské, G., Kaneko, T., Higashi, K., Yoshida, Y., Zhao, X., Sakata, T., Yamamoto, T., Gunji, T., Uruga, T. & Iwasawa, Y. (2018). *Appl. Mater. Interfaces*, **10**, 27734–27744.
Takao, S., Sekizawa, O., Samjeské, G., Nagamatsu, S., Kaneko, T., Yamamoto, T., Higashi, K., Nagasawa, K., Uruga, T. & Iwasawa, Y. (2015). *J. Phys. Chem. Lett.* **6**, 2121–2126.
Tamasaku, K., Tanaka, Y., Yabashi, M., Yamazaki, H., Kawamura, N., Suzuki, M. & Ishikawa, T. (2001). *Nucl. Instrum. Methods Phys. Res. A*, **467–468**, 686–689.
Teo, B. K. (1986). *EXAFS: Basic Principles and Data Analysis.* Springer-Verlag.
Thibault, P., Dierolf, M., Bunk, O., Menzel, A. & Pfeiffer, F. (2009). *Ultramicroscopy*, **109**, 338–343.
Thibault, P., Dierolf, M., Menzel, A., Bunk, O., David, C. & Pfeiffer, F. (2008). *Science*, **321**, 379–382.
Villar, F., Andre, L., Baker, R., Bohic, S., da Silva, J. C., Guilloud, C., Hignette, O., Meyer, J., Pacureanu, A., Perez, M., Salome, M., van der Linden, P., Yang, Y. & Cloetents, P. (2018). *Synchrotron Radiat. News* **31**, 9–14.
Vine, D. J., Pelliccia, D., Holzner, C., Baines, S. B., Berry, A., McNulty, I., Vogt, S., Peele, A. G. & Nugent, K. A. (2012). *Opt. Express*, **20**, 18287–18296.
Wise, A. M., Weker, J. N., Kalirai, S., Farmand, M., Shapiro, D. A., Meirer, F. & Weckhuysen, B. M. (2016). *ACS Catal.* **6**, 2178–2181.
Yamauchi, K., Mimura, H., Inagaki, K. & Mori, Y. (2002). *Rev. Sci. Instrum.* **73**, 4028–4033.
Yu, Y.-S., Farmand, M., Kim, C., Liu, Y., Grey, C. P., Strobridge, F. C., Tyliszczak, T., Celestre, R., Denes, P., Joseph, J., Krishnan, H., Maia, F., Kilcoyne, A. L. D., Marchesini, S., Leite, T. P. C., Warwick, T., Padmore, H., Cabana, J. & Shapiro, D. A. (2018). *Nat. Commun.* **9**, 921.
Yu, Y.-S., Kim, C., Shapiro, D. A., Farmand, M., Qian, D., Tyliszczak, T., Kilcoyne, A. L. D., Celestre, R., Marchesini, S., Joseph, J., Denes, P., Warwick, T., Strobridge, F. C., Grey, C. P., Padmore, H., Meng, Y. S., Kostecki, R. & Cabana, J. (2015). *Nano Lett.* **15**, 4282–4288.